



# A Variable Eddington Factor method for the 1-D grey radiative transfer equations with discontinuous Galerkin and mixed finite-element spatial differencing

Jijie Lou<sup>a,\*</sup>, Jim E. Morel<sup>a</sup>, N.A. Gentile<sup>b</sup>

<sup>a</sup> Department of Nuclear Engineering, Texas A&M University, College Station, TX 77843, USA

<sup>b</sup> Lawrence Livermore National Laboratory, P.O. Box 808, Livermore, CA 94550, USA

## ARTICLE INFO

### Article history:

Received 25 September 2018

Received in revised form 21 March 2019

Accepted 8 May 2019

Available online 13 May 2019

### Keywords:

Variable Eddington Factor

Quasi-diffusion

Discontinuous Galerkin

Mixed finite-element

## ABSTRACT

The purpose of this paper is to present a Variable Eddington Factor (VEF) method for the 1-D grey radiative transfer equations that uses a lumped linear discontinuous Galerkin spatial discretization for the  $S_n$  equations together with a constant-linear mixed finite-element discretization for the VEF moment and material temperature equations. The use of independent discretizations can be particularly useful for multiphysics applications such as radiation-hydrodynamics. The VEF method is quite old, but to our knowledge, this particular combination of differencing schemes has not been previously investigated for radiative transfer. We define the scheme and present computational results. As expected, the scheme exhibits second-order accuracy for the directionally-integrated intensity and material temperature, and behaves well in the thick diffusion limit. An important focus of this study is the treatment of the strong temperature dependence of the opacities and the spatial dependence of the opacities within each cell, which are not explicitly defined by the basic discretization schemes.

© 2019 Elsevier Inc. All rights reserved.

## 1. Introduction

The Variable Eddington Factor (VEF) method, also known as Quasi-Diffusion (QD) [1–3], was one of the first nonlinear methods for accelerating source iterations in  $S_n$  calculations [4]. It is comparable in effectiveness to both linear and nonlinear forms of Diffusion Synthetic Acceleration (DSA), but it offers much more flexibility than DSA. Stability can only be guaranteed with DSA if the diffusion equation is differenced in a manner consistent with that of the  $S_n$  equations [5]. Modern  $S_n$  codes often use advanced discretization schemes such as Discontinuous Galerkin (DG) since classic discretization schemes such as step and diamond are not suitable for radiative transfer (RT) calculations in the high energy density laboratory physics (HEDLP) regime, or for coupled electron-photon calculations. Diffusion discretizations consistent with DG  $S_n$  discretizations generally cannot be expressed in diffusion form, but rather must be expressed in first-order or  $P_1$  form, and are much more difficult to solve than standard diffusion discretizations [6]. Considerable effort has gone into the development of “partially consistent” diffusion discretizations that yield a stable DSA algorithm with some degree of degraded effectiveness, but such discretizations are also generally difficult to develop [7–9].

\* Corresponding author.

E-mail addresses: [loujijie1991@email.tamu.edu](mailto:loujijie1991@email.tamu.edu) (J. Lou), [morel@tamu.edu](mailto:morel@tamu.edu) (J.E. Morel), [gentile1@llnl.gov](mailto:gentile1@llnl.gov) (N.A. Gentile).

A great advantage of the VEF method is that the moment equations that accelerate the  $S_n$  source iterations can be discretized in any valid manner without concern for consistency with the  $S_n$  discretization. When the VEF moment equations are discretized in an independent way that is not consistent with the  $S_n$  discretization, the  $S_n$  and moment solutions for the directionally-integrated intensity and radiative flux do not necessarily become identical when the iterative process converges. However, they do become identical in the limit as the spatial mesh is refined, and the difference between the two solutions is a function of the difference in truncation errors for each discretization. In general, the order accuracy of the  $S_n$  and VEF moment solutions will be the lowest order accuracy of their respective independent discretizations. Although the  $S_n$  solution obtained with such an independently-discretized VEF method is not conservative, the VEF moment equations solutions are in fact conservative. This is particularly useful in multiphysics calculations where the low-dimensional moment equations can be coupled to the other physics components rather than the high-dimensional  $S_n$  equations. Another advantage of the independently-discretized approach is that even if the  $S_n$  spatial discretization scheme when applied in isolation does not preserve the thick diffusion limit [10], that limit will generally be preserved using the VEF method.

The purpose of this paper is to investigate the application of the VEF method to the 1-D slab-geometry equations of grey radiative transfer (RT) in the HEDLP regime with a particular form of the trapezoidal BDF2 temporal discretization [11] applied in conjunction with independent spatial discretizations for certain of the equations as opposed to one type of spatial discretization for all of the equations. In particular, the  $S_n$  transport equation is discretized with a Lumped Linear Discontinuous Galerkin (LLDG) method, while the moment equations and the material temperature equation are discretized using a constant-linear Mixed Finite-Element Method (MFEM). To our knowledge, this combination has not been previously investigated for RT, but it has been investigated for the steady-state neutron transport equation by Olivier and Morel [12]. That study was preliminary to the present study. Significant complications are introduced for the RT equations by the strong nonlinear dependencies upon material temperature of those equations, and the treatments for these nonlinearities are not necessarily defined by the basic FEM methods. Our motivation for this investigation is that MFEM methods are now being used for high-order hydrodynamics calculations at Lawrence Livermore National Laboratory (LLNL) [13]. A radiation transport method compatible with MFEM methods is clearly desirable for developing a MFEM radiation-hydrodynamics code. Such a code would combine thermal radiation transport with hydrodynamics. However, MFEM methods are inappropriate for the standard first-order form of the transport equation. Thus, the use of the VEF method with a DG  $S_n$  discretization and a MFEM discretization for the moment and material temperature equations suggests itself. Only the moment equation would be directly coupled to the hydrodynamics equations, with the material temperature equation replaced by either an internal or total material energy equation.

Here we define a VEF method that should exhibit second-order accuracy since both the transport and moment discretizations when applied in isolation are second-order accurate. In addition, our VEF method should preserve the thick diffusion limit, which is essential for radiative transfer calculations in the HEDLP regime. We use a lumped rather than standard linear discontinuous Galerkin discretization because lumping yields a much more robust scheme, and robustness is essential for radiative transfer calculations in the HEDLP regime. A major component of the present study is to address the treatment of the strong temperature dependence of the cross sections and the spatial representation of the cross sections, within each cell, neither of which are strictly defined by the basic discretization schemes. Since the moment equation becomes equivalent to a pure diffusion equation in the diffusion limit, a major requirement of our approach is to ensure that the discretization for the moment equations becomes symmetric-positive definite in this limit. The remainder of this paper is organized as follows. First, we describe the analytic equations of radiative transfer, followed by a description of the analytic VEF equations. We then describe several discrete variants of these VEF equations. Next we give computational results, and recommend one discrete variant based upon those results. Finally, we give conclusions and recommendations for future work.

## 2. The equations of radiative transfer

In this section we describe the 1-D slab-geometry equations of grey radiative transfer. These equations can be expressed as follows:

$$\frac{1}{c} \frac{\partial \psi}{\partial t} + \mu \frac{\partial \psi}{\partial x} + \sigma_t \psi = \frac{\sigma_s}{4\pi} \phi + \frac{\sigma_a}{4\pi} a c T^4, t \in [0, \infty), x \in [x_L, x_R], \quad (2.1)$$

$$C_v \frac{\partial T}{\partial t} = \sigma_a (\phi - a c T^4), t \in [0, \infty), x \in [x_L, x_R], \quad (2.2)$$

where  $c = 2.9979 \times 10^2$  cm/sh is the speed of light,  $t$  is time (sh),  $x$  is spatial position (cm),  $\mu$  is the  $x$  cosine of the photon direction vector,  $\psi(t, x, \mu)$  is the photon angular intensity (j/cm<sup>2</sup> sh steradian),  $\sigma_t = \sigma_s + \sigma_a$  is the macroscopic total cross section (cm<sup>-1</sup>),  $\sigma_s$  is the macroscopic Thompson scattering cross section (cm<sup>-1</sup>),  $\sigma_a$  is the macroscopic absorption cross section (cm<sup>-1</sup>),  $a = 0.01372$  j/cm<sup>3</sup> keV<sup>4</sup> is the radiation constant,  $T$  is the material temperature (keV),  $C_v$  is the heat capacity (j/cm<sup>3</sup> keV), and  $\phi(t, x)$  is the directionally-integrated intensity:

$$\phi = 2\pi \int_{-1}^{+1} \psi d\mu. \quad (2.3)$$

One jerk (j) is equal to  $10^9$  joules, and one shake (sh) is equal to  $10^{-8}$  seconds. Macroscopic cross sections are just opacities ( $\text{cm}^2/\text{g}$ ) multiplied by the material density ( $\text{g}/\text{cm}^3$ ). For simplicity we directly define macroscopic cross sections rather than opacities since the material density in our equations does not change in time. However, one has to define opacities when solving the radiation-hydrodynamics equations. The absorption cross section is generally strongly dependent upon temperature, while the scattering cross section and heat capacity are very weak functions of temperature. Equation (2.1) is the radiation transport equation, and Eq. (2.2) is the material internal energy or temperature equation. Equations (2.1) and (2.2) have the following initial conditions:

$$\psi(t, x, \mu) = \psi_0(x, \mu), t = 0, x \in [x_L, x_R], \quad (2.4)$$

$$T(t, x) = T_0(x), t = 0, x \in [x_L, x_R]. \quad (2.5)$$

Eq. (2.1) can have various boundary conditions:

$$\begin{aligned} \psi(t, x_L, \mu) &= \psi_L(t, \mu), \quad \mu > 0, \text{ source}, \\ &= \psi(t, x_L, -\mu), \quad \mu > 0, \text{ reflective}, \\ &= \psi(t, x_R, \mu), \quad \mu > 0, \text{ periodic}, \end{aligned} \quad (2.6)$$

and

$$\begin{aligned} \psi(t, x_R, \mu) &= \psi_R(t, \mu), \quad \mu < 0, \text{ source}, \\ &= \psi(t, x_R, -\mu), \quad \mu < 0, \text{ reflective}, \\ &= \psi(t, x_L, \mu), \quad \mu < 0, \text{ periodic}. \end{aligned} \quad (2.7)$$

If we integrate Eq. (2.1) over all directions, we get the radiation energy equation:

$$\frac{1}{c} \frac{\partial \phi}{\partial t} + \frac{\partial F}{\partial x} + \sigma_a \phi = \sigma_a a c T^4, t \in [0, \infty), x \in [x_L, x_R], \quad (2.8)$$

where  $F$  is the radiative flux,

$$F = 2\pi \int_{-1}^{+1} \mu \psi d\mu. \quad (2.9)$$

If we multiply Eq. (2.1) by  $\frac{\mu}{c}$  and integrate over all directions, we get the radiation momentum equation:

$$\frac{1}{c^2} \frac{\partial F}{\partial t} + \frac{\partial P}{\partial x} + \frac{\sigma_t}{c} F = 0, t \in [0, \infty), x \in [x_L, x_R], \quad (2.10)$$

where  $P$  is the radiation pressure:

$$P = \frac{1}{c} 2\pi \int_{-1}^{+1} \mu^2 \psi d\mu. \quad (2.11)$$

Eqs. (2.8) and (2.10) have the following initial conditions:

$$\phi(t, x) = 2\pi \int_{-1}^{+1} \psi_0(x, \mu) d\mu, t = 0, x \in [x_L, x_R], \quad (2.12)$$

$$F(t, x) = 2\pi \int_{-1}^{+1} \mu \psi_0(x, \mu) d\mu, t = 0, x \in [x_L, x_R]. \quad (2.13)$$

The boundary conditions for Eqs. (2.8) and (2.10) are presented in the next section after they are closed by the VEF equations.

Note that Eqs. (2.2), (2.8), and (2.10) can be closed by expressing the radiation pressure in terms of the directionally-integrated intensity. This is often done in an approximate manner. For instance, the diffusion approximation follows from the assumption that  $P = \frac{\phi}{3c}$ .

### 3. The analytic VEF equations

In this section we describe the analytic VEF equations. The VEF method is based in part upon an exact but trivial closure of Eqs. (2.2), (2.8), and (2.10):

$$P = f \frac{\phi}{c}, \quad (3.1)$$

where the variable Eddington factor,  $f$ , is defined by

$$f = \frac{2\pi \int_{-1}^{+1} \mu^2 \psi d\mu}{2\pi \int_{-1}^{+1} \psi d\mu} = P \frac{c}{\phi}. \quad (3.2)$$

Note that  $f$  is just the angular intensity-weighted average value of  $\mu^2$ . This closure is trivial because it is just an identity, thus one must know the angular intensity to compute  $f$ . Nonetheless, it is useful for achieving a rapid iterative solution of the radiative transfer equations. In particular, the VEF iteration equations can be written as follows, where  $\ell$  is the iteration index:

$$\frac{1}{c} \frac{\partial \psi^{\ell+1/2}}{\partial t} + \mu \frac{\partial \psi^{\ell+1/2}}{\partial x} + \sigma_t^\ell \psi^{\ell+1/2} = \frac{\sigma_s}{4\pi} \phi^\ell + \frac{\sigma_a^\ell}{4\pi} acT^{4,\ell}, \quad (3.3)$$

$$f^{\ell+1/2} = \frac{1}{\phi^{\ell+1/2}} 2\pi \int_{-1}^{+1} \mu^2 \psi^{\ell+1/2} d\mu, \quad (3.4)$$

$$\frac{1}{c} \frac{\partial \phi^{\ell+1}}{\partial t} + \frac{\partial F^{\ell+1}}{\partial x} + \sigma_a^{\ell+1} \phi^{\ell+1} = \sigma_a^{\ell+1} acT^{4,\ell+1}, \quad (3.5)$$

$$\frac{1}{c} \frac{\partial F^{\ell+1}}{\partial t} + \frac{\partial}{\partial x} [f^{\ell+1/2} \phi^{\ell+1}] + \sigma_t^{\ell+1} F^{\ell+1} = 0, \quad (3.6)$$

$$C_v \frac{\partial T^{\ell+1}}{\partial t} = \sigma_a^{\ell+1} (\phi^{\ell+1} - acT^{4,\ell+1}). \quad (3.7)$$

Note that Eq. (3.6) is just the radiation momentum equation multiplied by  $c$  for simplicity. We refer to it as the simplified radiation momentum equation. We collectively refer to Eqs. (3.5) and (3.6) as the moment equations. The boundary conditions for the moment equations are defined as: for a reflective condition,

$$F(t, x_L/x_R) = 0, \quad (3.8)$$

for a source condition,

$$F(t, x_L) = 2F^+(t, x_L) - f_{t,x_L}^b \phi(t, x_L), \quad (3.9)$$

$$F(t, x_R) = f_{t,x_R}^b \phi(t, x_R) - 2F^-(t, x_R), \quad (3.10)$$

where  $F^+ = 2\pi \int_0^1 \mu \psi d\mu$ ,  $F^- = -2\pi \int_{-1}^0 \mu \psi d\mu$  and

$$f_{t,x_L/x_R}^b = \frac{2\pi \int_{-1}^1 |\mu| \psi(t, x_L/x_R) d\mu}{2\pi \int_{-1}^1 \psi(t, x_L/x_R) d\mu}. \quad (3.11)$$

The VEF method can be characterized in the modern vernacular as a high-order/low-order (HOLO) method. When used in this context, “order” refers to “dimensionality” rather than “order accuracy”. The transport equation is the high-dimensional equation and the moment and temperature equations comprise the low-dimensional system. The low-dimensional system provides the transport equation with directionally-integrated intensities and temperatures, while the transport equation provides the low-dimensional system with Eddington factors. The VEF iteration process can be described as follows:

1. Invert the left side of the transport equation using the directionally-integrated intensities and temperatures from the previous iteration. When an  $S_n$  angular discretization is used with an appropriate spatial discretization, this inversion is easy to carry out. In particular, one need only solve an independent block lower-triangular system for each direction. This solution process is called a sweep because one literally sweeps through the mesh in the direction of radiation flow, sequentially solving for the intensities in each cell.
2. Compute the Eddington factors using the  $S_n$  sweep solution for the angular intensities.
3. Solve the moment and temperature equations using these variable Eddington factors.

4. Use the directionally-integrated intensities and temperatures to construct the right scattering and emission sources for the transport equation, and return to Step 1.

Note that the high-order solution process is linear, while the low-order solution process is nonlinear. Thus the low-order equations must themselves be solved iteratively, resulting in an overall nested iteration process with the VEF iterations on the outside. It is not necessary to fully converge the nonlinearities in the low-order solve before doing another transport sweep, but it is not clear what is optimal in this regard. We do not address this question here, but rather focus on discretization issues related to the nonlinearities. Hence, here we converge the nonlinearities in the low-order solution after each sweep.

The inner iteration scheme we use to solve the low-order equations is straightforward. In particular, the temperature dependence of the radiation emission source is linearized, but the temperature dependence of the opacities is simply lagged:

$$\frac{1}{c} \frac{\partial \phi^{l+1}}{\partial t} + \frac{\partial F^{l+1}}{\partial x} + \sigma_a^l \phi^{l+1} = \sigma_a^l \left[ acT^{4,l} + 4acT^{3,l} (T^{l+1} - T^l) \right], \quad (3.12)$$

$$\frac{1}{c} \frac{\partial F^{l+1}}{\partial t} + \frac{\partial}{\partial x} [f^{\ell+1/2} \phi^{l+1}] + \sigma_t^l F^{l+1} = 0, \quad (3.13)$$

$$C_v \frac{\partial T^{l+1}}{\partial t} = \sigma_a^l \left[ \phi^{\ell+1} - acT^{4,l} - 4acT^{3,l} (T^{l+1} - T^l) \right], \quad (3.14)$$

where  $l$  is the iteration index. Next  $T^{l+1}$  is algebraically eliminated from Eq. (3.12) using Eq. (3.14). Given our temporal and spatial discretization schemes, this results in two coupled banded matrix systems that can be directly inverted. Once the intensities and fluxes have been obtained, a local system is solved for the temperatures. This process is later described in greater detail in terms of the discretized equations.

#### 4. The TR/BDF2 method

A non-standard form of TR/BDF2 method is used for the time differencing scheme [14]. Applying this scheme to the following equation:

$$\frac{\partial u}{\partial t} = \mathbf{A}u, \quad (4.1)$$

we obtain

$$\frac{2(u^{n+1/2} - u^n)}{\Delta t_n} = \frac{1}{2} \mathbf{A}^{n+1/2} u^{n+1/2} + \frac{1}{2} \mathbf{A}^n u^n, \quad (4.2a)$$

$$\frac{2(u^{n+1} - u^{n+1/2})}{\Delta t_n} = \frac{2}{3} \mathbf{A}^{n+1} u^{n+1} + \frac{1}{6} \mathbf{A}^{n+1/2} u^{n+1/2} + \frac{1}{6} \mathbf{A}^n u^n, \quad (4.2b)$$

where  $\Delta t_n$  is the time step from  $t_n$  to  $t_{n+1}$ . Note, each equation represents a conservation statement over each half time step, respectively. A modified form is also used for the following equation:

$$\mathbf{C} \frac{\partial u}{\partial t} = \mathbf{A}u, \quad (4.3)$$

we obtain

$$\mathbf{C}^{n+1/4} \frac{2(u^{n+1/2} - u^n)}{\Delta t_n} = \frac{1}{2} \mathbf{A}^{n+1/2} u^{n+1/2} + \frac{1}{2} \mathbf{A}^n u^n, \quad (4.4a)$$

$$\mathbf{C}^{n+3/4} \frac{2(u^{n+1} - u^{n+1/2})}{\Delta t_n} = \frac{2}{3} \mathbf{A}^{n+1} u^{n+1} + \frac{1}{6} \mathbf{A}^{n+1/2} u^{n+1/2} + \frac{1}{6} \mathbf{A}^n u^n. \quad (4.4b)$$

#### 5. The discrete ordinates angular discretization

Applying the discrete ordinates ( $S_n$ ) angular discretization for Eq. (3.3) leads to the following set of  $M$  coupled, ordinary differential equations:

$$\frac{1}{c} \frac{\partial \psi_m^{l+1/2}}{\partial t} + \mu_m \frac{\partial \psi_m^{l+1/2}}{\partial x} + \sigma_t^l \psi_m^{l+1/2} = \frac{\sigma_s}{4\pi} \phi^l + \frac{\sigma_a^l}{4\pi} acT^{4,l}, \quad 1 \leq m \leq M, \quad (5.1)$$

where  $\psi_m(x) = \psi(x, \mu_m)$  is the photon angular intensity with directions within the ring of points on the unit sphere defined by  $\mu_m$ . The cosines,  $\{\mu_m\}_{m=1}^M$ , are defined by an  $M$ -point Gauss quadrature rule in which the directionally-integrated intensity,  $\phi(t, x)$ , is numerically integrated as follows:

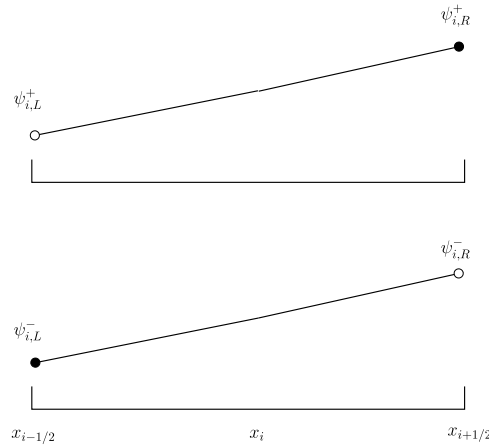


**Fig. 1.** The spatial dependence of unknowns within a LLDG cell. The superscript + and – indicate the angular fluxes for  $\mu_m > 0$  and  $\mu_m < 0$ , respectively.

$$\phi(t, x) = \sum_{m=1}^M \psi_m(t, x) w_m, \quad (5.2)$$

where  $w_m$  is the quadrature weight corresponding to  $\mu_m$ .

## 6. Lumped linear discontinuous Galerkin $S_N$

The spatial domain is discretized into  $I$  cells. The indices for cell centers are integral and the indices for cell edges are half integral. The spatial dependence of unknowns for an LLDG cell  $i$  is plotted in Fig. 1.

The two unknowns for cell  $i$  with discrete direction  $\mu_m$  are the  $\psi_{i,m,L}$  and  $\psi_{i,m,R}$ , where  $i$  is the cell index, and  $m$  is the discrete direction index. The angular intensity dependence within cells is linear and is given in cell  $i$  by

$$\psi_{i,m}(x) = \psi_{i,m,L} B_{i,L}(x) + \psi_{i,m,R} B_{i,R}(x), \quad x \in (x_{i-1/2}, x_{i+1/2}), \quad (6.1)$$

where the LLDG basis functions are defined as:

$$B_{i,L}(x) = \begin{cases} \frac{x_{i+1/2}-x}{x_{i+1/2}-x_{i-1/2}}, & x \in [x_{i-1/2}, x_{i+1/2}] \\ 0, & \text{otherwise} \end{cases}, \quad (6.2a)$$

$$B_{i,R}(x) = \begin{cases} \frac{x-x_{i-1/2}}{x_{i+1/2}-x_{i-1/2}}, & x \in [x_{i-1/2}, x_{i+1/2}] \\ 0, & \text{otherwise} \end{cases}. \quad (6.2b)$$

The cell centered angular intensity is the average of the left and right discontinuous interior-edge intensities:

$$\psi_{i,m} = \frac{1}{2}(\psi_{i,m,L} + \psi_{i,m,R}). \quad (6.3)$$

The interface or cell-edge intensities are uniquely defined in terms of the interior-edge intensities by upwinding:

$$\psi_{i-1/2,m}(x) = \begin{cases} \psi_{i-1,m,R}, & \mu_m > 0 \\ \psi_{i,m,L}, & \mu_m < 0 \end{cases}, \quad (6.4a)$$

$$\psi_{i+1/2,m}(x) = \begin{cases} \psi_{i,m,R}, & \mu_m > 0 \\ \psi_{i+1,m,L}, & \mu_m < 0 \end{cases}. \quad (6.4b)$$

We first assume the scattering and emission source in Eq. (5.1) to be constant within each cell defined by the MFEM equations. The detailed spatial discretization is included in Appendix A.

## 7. Mixed Finite-Element method for Low Order system

MFEM method is applied to the lower order system composed of Eqs. (3.5), (3.6) and (3.7). In MFEM, separate basis functions are used for the directionally-integrated intensity and radiative flux. The spatial dependence of the radiative unknowns within cell  $i$  in the MFEM method is plotted in Fig. 2.

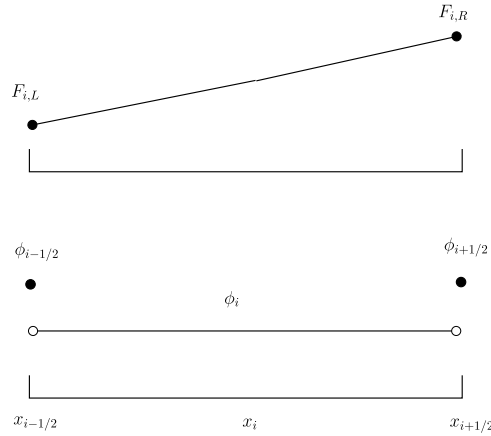


**Fig. 2.** The spatial dependence of the unknowns within a MFEM cell.

The directionally-integrated intensity is constant within a cell with discontinuous jumps at the cell edges. In other words,

$$\phi_i(x) = \begin{cases} \phi_i, & x \in (x_{i-1/2}, x_{i+1/2}) \\ \phi_{i\pm 1/2}, & x = x_{i\pm 1/2} \\ 0, & \text{otherwise} \end{cases} \quad (7.1)$$

The material temperatures have the same piecewise-constant dependence within each cell as the directionally-integrated intensities, but they do not jump at the cell edges because the temperature equation has no spatial derivatives. Thus, the temperatures are undefined at the cell edges.

Since the LLDG and MFEM approximations use the same spatial grid, the Eddington factors are available at any space point as required for the MFEM equations.

The radiative flux,  $F_i(x)$ , is a piecewise linear function defined by

$$F_i(x) = F_{i,L} B_{i,L}(x) + F_{i,R} B_{i,R}(x), \quad (7.2)$$

where  $F_{i,L}$  and  $F_{i,R}$  are the radiative fluxes on the left and right edges of the cell  $i$ , respectively, and the basis functions are the same as the ones defined by Eqs. (6.2a) and (6.2b) for the LLDG  $S_n$  discretization. This constant-linear MFEM has second-order accuracy for both the directionally-integrated intensity and the radiative flux. Also, the temperature is piecewise constant within each cell,  $T_i$ , in accordance with the spatial dependence of  $\phi_i$  and the desired equilibrium solution,  $\phi = acT^4$ .

The MFEM representation has 6 unknowns per cell:  $\phi_{i-1/2}$ ,  $\phi_i$ ,  $\phi_{i+1/2}$ ,  $F_{i,L}$ ,  $F_{i,R}$  and  $T_i$ , but the cell-edge directionally-integrated intensity is shared by two cells, therefore, for  $I$  cells, there is a total of  $I$  cell-centered directionally-integrated intensities,  $I$  temperatures,  $2I$  radiative fluxes,  $2I - 1$  interior cell-edge directionally-integrated intensities, and 2 boundary directionally-integrated intensities. The sequence for solving the low order system can be described as follows: the expression for  $T_i$  is obtained from Eq. (3.14), then  $T_i$  is eliminated from Eq. (3.12), which yields the equation for  $\phi_i$ . Equations for  $F_{i,L/R}$  are obtained by multiplying Eq. (3.13) by  $B_{i,L/R}$  and integrating over cell  $i$ . Substituting the expression of  $F_{i,L/R}$  back into the radiation energy equation and imposing continuity of the flux at the cell edge yields the equations for the cell-center directionally-integrated intensities and the interior cell-edge directionally-integrated intensities, respectively. A detailed discretization process is included in Appendix B.

Note that the MFEM defines the directionally-integrated intensity to be constant within each cell, while LLDG defines the directionally-integrated intensity to be linear within each cell. This suggests that improved accuracy for the  $S_n$  solution may be achieved by constructing a linear dependence within each cell via slope reconstruction from the MFEM solutions for the scattering and emission source. We applied such a slope reconstruction process and tested it for a 1-D Marshak wave problem.

## 8. Computational results

### 8.1. Method of Manufacture Solutions

The Method of Manufactured Solutions (MMS) is used to test the time and spatial accuracy of our scheme as the time step and cell width are decreased. The spatial domain for the manufactured solution is  $[-x_0, +x_0]$  with  $x_0 = 10$  cm, the absorption cross section is  $\sigma_a = 1 \text{ cm}^{-1}$ , the heat capacity is  $4aT^3 \text{ j/cm}^3 - \text{keV}$ , the initial angular intensity is isotropic

with an directionally-integrated value of  $\phi_0 = acT_0^4$ , with  $T_0 = 1$  keV, and there is no scattering. The solutions are chosen as follows:

$$\begin{aligned}\psi(x, \mu, t) &= \frac{1}{2\pi}(-x^2 + x_0^2)(1 + \frac{x}{x_0}\mu)[\frac{ct}{2} + \frac{1}{4\sigma_a}(1 - \exp(-2\sigma_a ct))] + \frac{\phi_0}{4\pi}, \\ \phi(x, t) &= 2(-x^2 + x_0^2)[\frac{ct}{2} + \frac{1}{4\sigma_a}(1 - \exp(-2\sigma_a ct))] + \phi_0, \\ T^4(x, t) &= 2(-x^2 + x_0^2)[\frac{ct}{2} - \frac{1}{4\sigma_a}(1 - \exp(-2\sigma_a ct))]/(ac) + T_0^4.\end{aligned}\quad (8.1)$$

Then the distributed radiation source has the following form:

$$\begin{aligned}q(x, \mu, t) &= \frac{\mu}{2\pi}[\frac{ct}{2} + \frac{1}{4\sigma_a}(1 - \exp(-2\sigma_a ct))]( -2x - \frac{3\mu x^2}{x_0} + x_0\mu) \\ &+ \frac{\mu}{2\pi}(-x^2 + x_0^2)\frac{x}{x_0}[\frac{3}{4} + \frac{\sigma_a ct}{2} + \frac{1}{4}\exp(-2\sigma_a ct)] \\ &+ \frac{1}{2\pi}(-x^2 + x_0^2).\end{aligned}\quad (8.2)$$

Note that the solution is constructed in a manner that there is no source for the material temperature equation.

The  $S_n$  calculations for this problem were solved with Gauss S8 quadrature. The calculation is terminated at  $t = 1.28 \times 10^{-5}$  sh. The time steps and cell widths for each problem are given by  $1.28 \times 10^{-7} \times (\frac{1}{2})^n$  sh and  $4 \times (\frac{1}{2})^n$  cm for  $n = (0, 1, 2, \dots, 6)$ . Thus we perform a series of calculations in which the time step and spatial cell widths are simultaneously reduced by a factor of 2 for each successive calculation. The  $L_2$  errors between the numerical and analytical solutions for  $\phi$  and  $T$  are computed for 7 successive calculations. Indeed, performing linear regression on the data for  $T$  and  $\phi$ , we obtain an order of convergence of 1.9640 with an  $R^2$  value of 0.99987 and an order of convergence of 1.998 with an  $R^2$  value of 0.99999, respectively.

## 8.2. Marshak wave problem

We also performed calculations for a Marshak wave problem. This test case consists of an isotropic black-body source at a temperature of 1 keV impinging on the left boundary of the slab. The slab has a thickness of 0.05 cm, an initial spatially-uniform temperature of 1 eV, and an isotropic black-body source at a temperature of 1 eV impinging on the right boundary. The slab material properties are defined by a temperature-dependent macroscopic absorption cross-section, a null scattering cross-section, and a constant heat capacity. The macroscopic absorption cross-section is given by  $\sigma_a = 300/(T^3)$  cm<sup>-1</sup> with  $T$  in keV. The heat capacity has a value of 0.3 j/cm<sup>3</sup> – keV. A constant time step size of  $\Delta t = 1.25 \times 10^{-6}$  shakes is used for all calculations with the number of spatial cells taking on values of 100, 200, 500, and 1000. It should be noted that while the cross section we define is not physically accurate, it provides a stringent test for any numerical radiative transfer method and makes our computational results easy to reproduce.

We stress that the opacities in the transport equation and the radiation energy equation are evaluated in each cell at the material temperature obtained for that cell from the solution of the material temperature equation. However, as previously discussed, Marshak waves cannot be accurately propagated with a reasonable number of spatial cells unless the opacities in the radiation momentum equation are evaluated in a special manner. We investigate two options for defining the opacity within each cell in this equation. In particular, let us denote the special temperature at which the opacity in cell  $i$  is evaluated by  $T_i^*$ , then,

- Option 1:

$$\begin{aligned}T_i^* &= \frac{1}{4}T_{i-1} + \frac{1}{2}T_i + \frac{1}{4}T_{i+1}, \quad i = 2, \dots, I-1, \\ T_1^* &= \frac{1}{2}T_L + \frac{1}{4}T_1 + \frac{1}{4}T_2, \quad T_I^* = \frac{1}{4}T_{I-1} + \frac{1}{4}T_I + \frac{1}{2}T_R,\end{aligned}\quad (8.3)$$

where  $T_{L/R}$  is the black body source temperature at the left/right boundary.

- Option 2:

$$\begin{aligned}T_i^* &= (\frac{1}{4}T_{i-1}^4 + \frac{1}{2}T_i^4 + \frac{1}{4}T_{i+1}^4)^{\frac{1}{4}}, \quad i = 2, \dots, I-1, \\ T_1^* &= (\frac{1}{2}T_L^4 + \frac{1}{4}T_1^4 + \frac{1}{4}T_2^4)^{\frac{1}{4}}, \quad T_I^* = (\frac{1}{4}T_{I-1}^4 + \frac{1}{4}T_I^4 + \frac{1}{2}T_R^4)^{\frac{1}{4}}.\end{aligned}\quad (8.4)$$



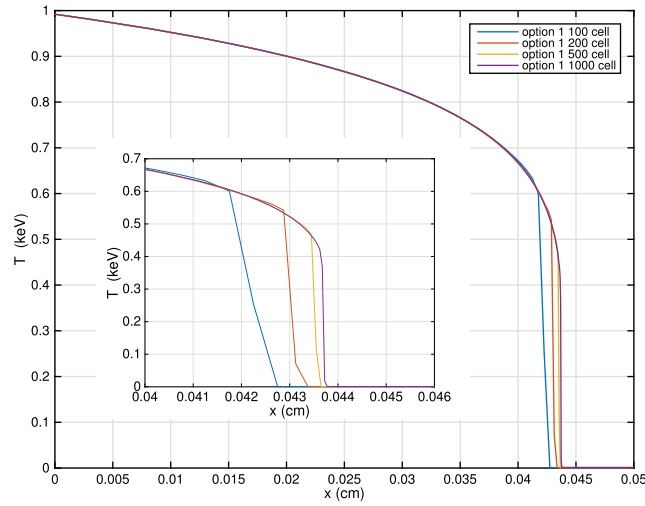


**Fig. 3.** The material temperature using Option 1 at  $t = 0.1$  shake.

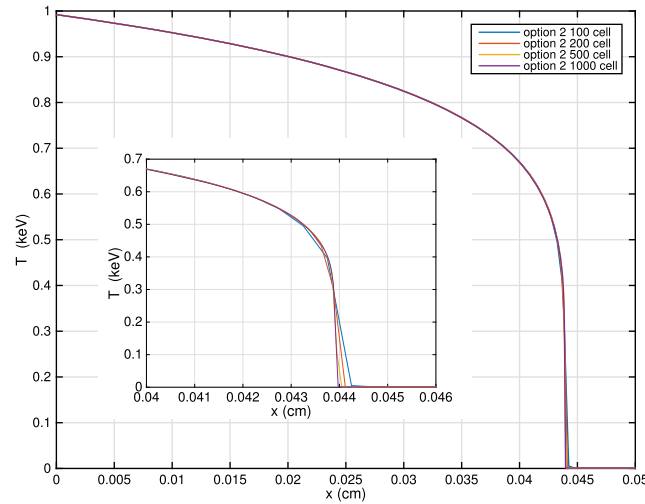


**Fig. 4.** The material temperature using Option 2 at  $t = 0.1$  shake.

The material temperatures at  $t = 0.1$  shake are plotted in Figs. 3 to 5. Note, the superimposed figures are just the magnification from domain  $[0.04, 0.046]$  cm. We also include the results from IMC method [15] as a popular reference for comparison, while recognizing that IMC has numerical error as well as statistical error. It can be seen from the figures that while both options converge with an increased number of cells, but Option 2 converges faster than Option 1 in terms of the overall position of the wave front. However, there is a one-cell-wide “glitch” in the Option 2 solution at the foot of the wave that is also present to a lesser extent in the IMC solution.

Spatial slope reconstruction for the emission source for the LLDG  $S_n$  equations is also investigated for the Marshak wave problem. Although we do not include scattering in this problem, we describe the full process that includes scattering. Assuming  $\sigma_a$  within cells is linear and is given in cell  $i$  by

$$\sigma_{a,i}(x) = \sigma_{a,i,L} B_{i,L}(x) + \sigma_{a,i,R} B_{i,R}(x), \quad x \in (x_{i-1/2}, x_{i+1/2}). \quad (8.5)$$

$\sigma_{a,i,L}$  and  $\sigma_{a,i,R}$  are evaluated at  $T_{i,L}$  and  $T_{i,R}$ , respectively. And  $T_{i,L}$  and  $T_{i,R}$  are defined as follows:

$$\begin{aligned} T_{i,L} &= (T_i^4 - T_{i,x}^4)^{1/4}, \\ T_{i,R} &= (T_i^4 + T_{i,x}^4)^{1/4}, \end{aligned} \quad (8.6)$$

where

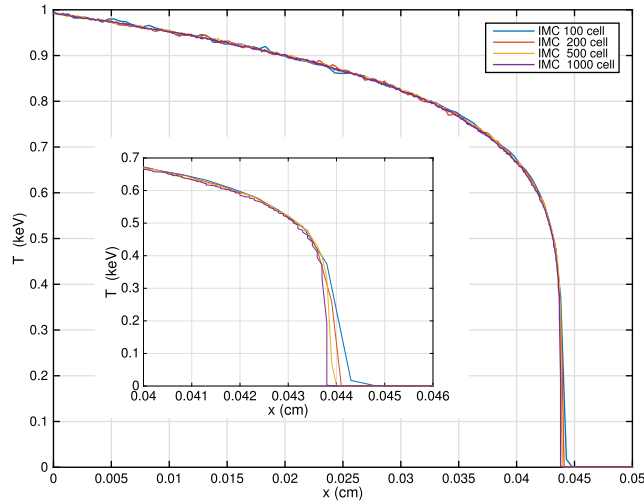


Fig. 5. The material temperature using IMC at  $t = 0.1$  shake.

$$\begin{aligned}
 T_{i+1/2}^4 &= \frac{T_i^4 + T_{i+1}^4}{2}, \quad i = 1, \dots, I-1, \\
 T_{i,x}^4 &= \frac{1}{2}(T_{i+1/2}^4 - T_{i-1/2}^4), \quad i = 2, \dots, I-1, \\
 T_{1,x}^4 &= T_{2,x}^4, \quad T_{I,x}^4 = T_{I-1,x}^4.
 \end{aligned} \tag{8.7}$$

Then the spatial dependence of the total cross section is given by

$$\begin{aligned}
 \sigma_{t,i}(x) &= \sigma_{a,i}(x) + \sigma_{s,i}, \quad x \in (x_{i-1/2}, x_{i+1/2}), \\
 \sigma_{t,i,L} &= \sigma_{a,i,L} + \sigma_{s,i}, \quad \sigma_{t,i,R} = \sigma_{a,i,R} + \sigma_{s,i}.
 \end{aligned} \tag{8.8}$$

We also assume the directionally-integrated intensity and temperature is linear within cells and is given in cell  $i$  by

$$\phi_i(x) = \phi_{i,L} B_{i,L}(x) + \phi_{i,R} B_{i,R}(x), \quad x \in (x_{i-1/2}, x_{i+1/2}), \tag{8.9}$$

$$T_i(x) = T_{i,L} B_{i,L}(x) + T_{i,R} B_{i,R}(x), \quad x \in (x_{i-1/2}, x_{i+1/2}). \tag{8.10}$$

$\phi_{i,L}$  and  $\phi_{i,R}$  is defined as follows:

$$\begin{aligned}
 \phi_{i,x} &= \frac{1}{2}(\phi_{i+1/2} - \phi_{i-1/2}), \\
 \phi_{i,L} &= \phi_i - \phi_{i,x}, \\
 \phi_{i,R} &= \phi_i + \phi_{i,x}.
 \end{aligned} \tag{8.11}$$

The material temperatures for the Marshak wave problem at  $t = 0.1$  sh are plotted in Fig. 6.

The difference between Option 2 and 3 is surprisingly negligible. This is encouraging since Option 2 is a lot simpler than Option 3.

We also performed the Marshak wave problem using all three options with only 10 cells to get some idea of the performance of these options with a coarse grid. The material temperatures corresponding to these options are plotted in Fig. 7. The results from Option 2 and 3 agree well with each other as expected. Compared to the previous results using 1000 cells, at  $t = 0.1$  sh, the temperature wave reaches a position around 0.044 cm. Here, Options 2 and 3 give nearly identical solutions. IMC propagates the wave faster than Options 2 and 3, but Option 1 is unacceptably inaccurate relative to the other methods.

### 8.3. The equilibrium diffusion limit

The VEF method is also tested in the equilibrium diffusion limit for several values of the asymptotic scaling parameter,  $\epsilon$ . The time derivative, cross sections, and material source are scaled as follows [16]:

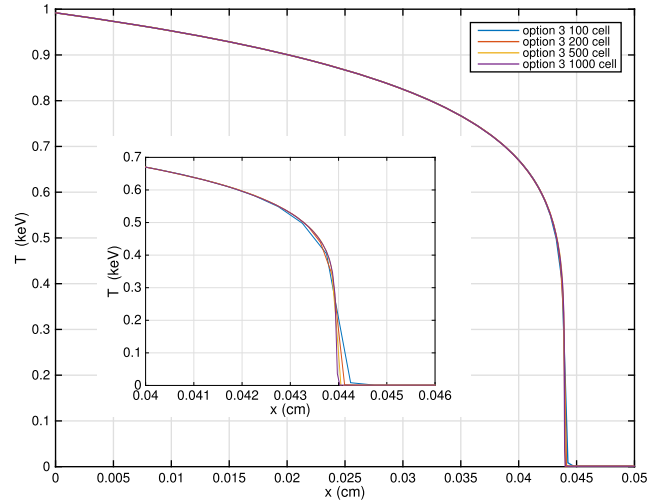


**Fig. 6.** The material temperature using the Option 3 at  $t = 0.1$  shake.

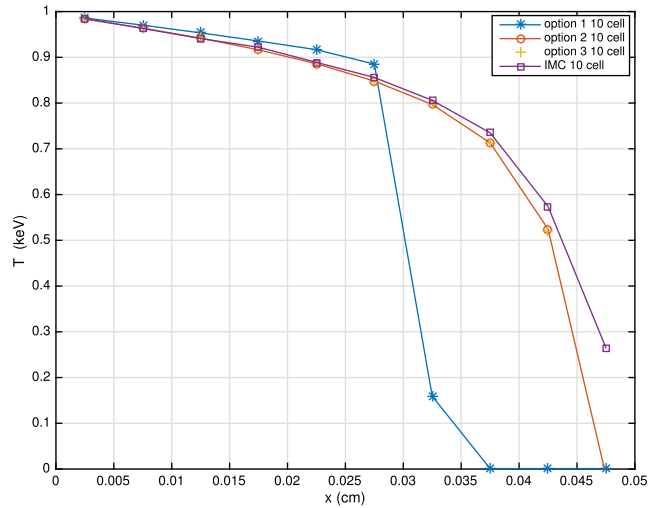


**Fig. 7.** The material temperature using three options at  $t = 0.1$  shake using 10 cells compared to IMC result.

$$\begin{aligned}
 \frac{d}{dt} &\rightarrow \epsilon \frac{d}{dt}, \\
 \sigma_t &\rightarrow \frac{\sigma_t}{\epsilon}, \\
 \sigma_a &\rightarrow \frac{\sigma_t}{\epsilon} - \sigma_s, \\
 Q &\rightarrow Q\epsilon,
 \end{aligned} \tag{8.12}$$

with  $\sigma_t = \sigma_a = 1$  cm,  $C_v = 1$  j/cm<sup>3</sup> keV and  $Q = 10$  j/cm<sup>3</sup> sh, where  $Q$  is a material energy source. The initial condition  $\phi_0 = acT^4$  is given as  $T_0 = 1$  keV. The time step is chosen as  $1 \times 10^{-5}$  sh, and the calculation is terminated as  $t = 1$  sh.  $\epsilon$  takes on values of 1, 0.1 and 0.01. As  $\epsilon \rightarrow 0$ , the system becomes diffusive. The VEF numerical solutions for the material temperature are compared with the analytic equilibrium diffusion solution in Fig. 8.

The results show that the VEF solution is essentially converging to the diffusion solution as  $\epsilon \rightarrow 0$ . Rigorous convergence cannot be expected since the VEF solution has truncation error. Nonetheless, these results clearly indicate the VEF method preserves the thick diffusion limit.

Another important property of transport discretizations in the thick diffusion limit is their behavior with spatially unresolved boundary layers. We have also tested our VEF method for this case. The test problem consists of slab of thickness 1 cm, with an initial spatially-uniform temperature of 1 keV. The slab material properties are defined by a constant absorption cross section of  $\sigma_a = 100$  cm<sup>-1</sup>, a null scattering cross-section, and a constant heat capacity with a value of  $10^{-2}$  j/cm<sup>3</sup> keV.

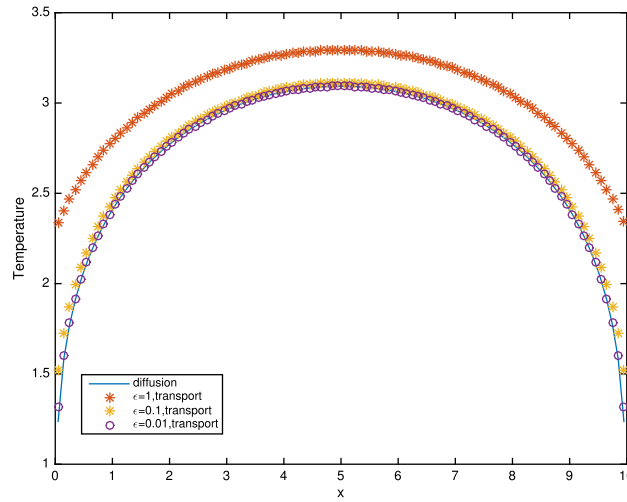


Fig. 8. The temperature using different scale values.

All calculations use Gauss S8 quadrature, a constant time step size of  $\Delta t = 5 \times 10^{-7}$  sh, and terminate at 0.002 sh. This is a highly diffusive problem. To generate a boundary layer we impose an incident flux at the left boundary with a highly anisotropic angular dependence. An isotropic dependence has no boundary layer to leading order. We perform four calculations:

1. a spatially resolved calculation with an isotropic flux incident,
2. a spatially unresolved calculation with an isotropic flux incident,
3. a spatially resolved calculation with an anisotropic flux incident, and
4. a spatially unresolved calculation with an anisotropic boundary flux incident.

The resolved calculations use 5000 spatial cells, while the unresolved calculations use 10 spatial cells. The angular intensity at the left boundary is defined as follows for  $t > 0$ :

- Isotropic case:

$$\psi(0, \mu, t) = \frac{acT^4}{4\pi}, \quad (8.13)$$

where  $T = 1.5$  KeV and  $\mu > 0$ . Then the incoming radiative flux is:

$$F^+(0, t) = 2\pi \int_0^1 \psi(0, \mu, t) \mu d\mu = \sum_{\mu_m > 0} \psi(0, \mu_m, t) \mu_m w_m. \quad (8.14)$$

- Anisotropic case:

$$\psi(0, \mu_1, 0) = \frac{F^+(0, t)}{\mu_1 w_1}, \quad (8.15)$$

where  $\mu_1$  is the quadrature point closest to 1.

The results for anisotropic case are plotted in Fig. 9. It is observed that the solutions for isotropic case agree well with the equilibrium diffusion solutions, while there is boundary layer in the directionally-integrated intensity solution for the anisotropic case. As expected for the isotropic case, the solutions for the spatially unresolved calculations are essentially identical to those for the resolved calculations. For the anisotropic case, the solutions are excellent on the interior and quite good on the boundary. In particular, at the boundary the solution for the unresolved directionally-integrated intensity is 14.52 j/cm<sup>2</sup> sh and is 14.02 j/cm<sup>2</sup> sh for the resolved case. More importantly, while not shown in the plots, the half-range reflected flux at the boundary for the unresolved calculation is 4.97 j/cm<sup>2</sup> sh and is 5.48 j/cm<sup>2</sup> sh for the resolved case. This is excellent behavior with an unresolved boundary layer.

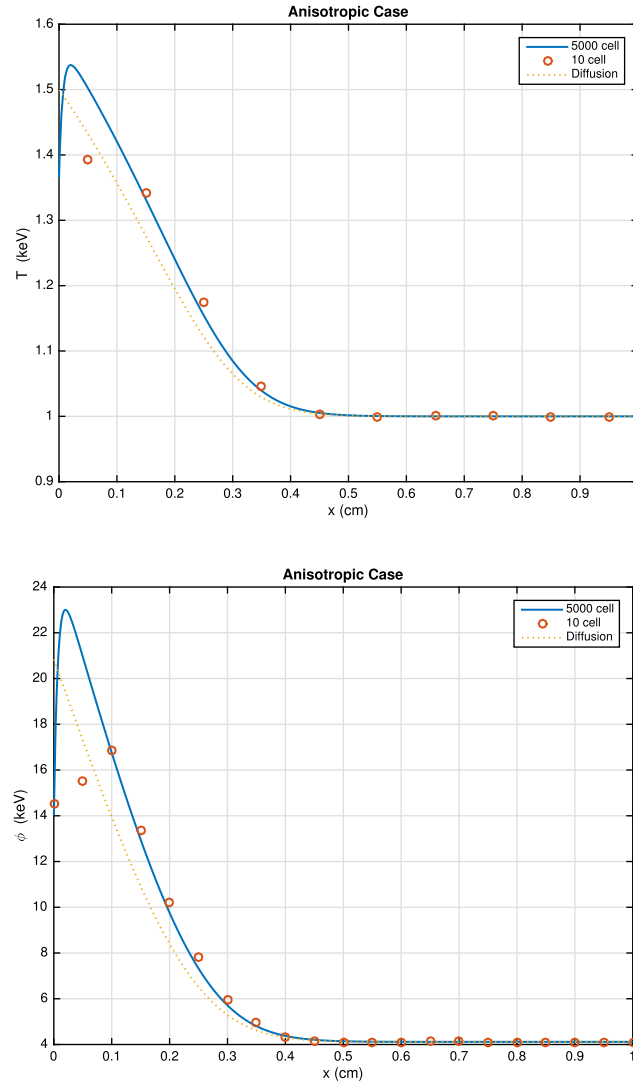


Fig. 9. The material temperature and directionally-integrated intensity at  $t = 0.002$  shake for anisotropic case.

## 9. Conclusions

We derived a VEF method for the 1D grey radiative transfer equation coupling  $S_n$  equations using an LLDG discretization with the moment and material energy equations using a MFEM discretization. The MMS was employed to generate a benchmark solution and the results show that the VEF method has second order accuracy in time and space. Moreover, the VEF method preserves the thick diffusion limit, and behaves well with an unresolved boundary layer. Two options for defining the opacity in the momentum equation were investigated for 1D Marshak wave problem. It was found that using the fourth-root of the average of  $T^4$  makes the solution converge faster than using the average of  $T$  for the opacity. We also investigated methods for representing the spatial dependence of the  $S_n$  scattering and emission sources given the solution from the lower order equations. The first option consists of using the flat native MFEM representation for source, while the second option consists using slope reconstruction together with the MFEM solution to generate linear discontinuous scattering and emission sources. However, for the test problem considered, the differences in solutions from those two methods are negligible. Overall, we recommend using the native piecewise-constant MFEM sources in the  $S_n$  equations together with the fourth-root of the average of  $T^4$  for evaluating opacities in the momentum equation. Most importantly, this VEF scheme showed rapid spatial convergence for Marshak wave problems, and is comparable in accuracy to IMC, even though the VEF emission source is flat in each cell. This is somewhat unexpected since it is well known that constructing a linear emission source is essential for accurate IMC solutions in Marshak wave problems [17].

In the future, we intend to develop a full VEF-based 1D radiation-hydrodynamics algorithm with an LLDG discretization for the  $S_n$  equations and MFEM discretizations for the moment, temperature, and hydrodynamic equations. We would also like to extend the present study to multi-D geometries with higher order discretizations.

## Acknowledgements

This work was performed under the auspices of the U.S. Department of Energy by Lawrence Livermore National Laboratory under Contract DE-AC52-07NA27344.

## Appendix A. Spatial Discretization for Lumped Linear Discontinuous Galerkin $S_n$

The lumped discretization equations are obtained by first integrating the spatial derivative terms by parts, and then performing all volumetric integrals using trapezoidal quadratures. The LLDG discretization of Eq. (3.3) for the first half time step is given by

$$\begin{aligned} \mu_m(\psi_{i,m}^{n+1/2,l+1/2} - \psi_{i-1/2,m}^{n+1/2,l+1/2}) + \frac{h_i}{2}(\frac{4}{c\Delta t_n} + \sigma_{t,i}^{n+1/2,l})\psi_{i,m,L}^{n+1/2,l+1/2} \\ = \frac{\sigma_{s,i}h_i}{8\pi}\phi_i^{n+1/2,l} + \frac{\sigma_{a,i}^{n+1/2,l}h_i}{8\pi}acT_i^{4,n+1/2,l} + Q_{i,m,L}^n, \end{aligned} \quad (A.1a)$$

$$\begin{aligned} \mu_m(\psi_{i+1/2,m}^{n+1/2,l+1/2} - \psi_{i,m}^{n+1/2,l+1/2}) + \frac{h_i}{2}(\frac{4}{c\Delta t_n} + \sigma_{t,i}^{n+1/2,l})\psi_{i,m,R}^{n+1/2,l+1/2} \\ = \frac{\sigma_{s,i}h_i}{8\pi}\phi_i^{n+1/2,l} + \frac{\sigma_{a,i}^{n+1/2,l}h_i}{8\pi}acT_i^{4,n+1/2,l} + Q_{i,m,R}^n, \end{aligned} \quad (A.1b)$$

where

$$Q_{i,m,L}^n = -\mu_m(\psi_{i,m}^n - \psi_{i-1/2,m}^n) + \frac{h_i}{2}(\frac{4}{c\Delta t_n} - \sigma_{t,i}^n)\psi_{i,m,L}^n + \frac{\sigma_{s,i}h_i}{8\pi}\phi_i^n + \frac{\sigma_{a,i}^nh_i}{8\pi}acT_i^{4,n}, \quad (A.2a)$$

$$Q_{i,m,R}^n = -\mu_m(\psi_{i+1/2,m}^n - \psi_{i,m}^n) + \frac{h_i}{2}(\frac{4}{c\Delta t_n} - \sigma_{t,i}^n)\psi_{i,m,R}^n + \frac{\sigma_{s,i}h_i}{8\pi}\phi_i^n + \frac{\sigma_{a,i}^nh_i}{8\pi}acT_i^{4,n}. \quad (A.2b)$$

Therefore, for  $\mu_m > 0$ :

$$\begin{aligned} \begin{bmatrix} \mu_m + (\sigma_{t,i}^{n+1/2,l} + \frac{4}{c\Delta t_n})h_i & \mu_m \\ -\mu_m & \mu_m + (\sigma_{t,i}^{n+1/2,l} + \frac{4}{c\Delta t_n})h_i \end{bmatrix} \begin{bmatrix} \psi_{i,m,L}^{n+1/2,l+1/2} \\ \psi_{i,m,R}^{n+1/2,l+1/2} \end{bmatrix} \\ = \begin{bmatrix} \frac{\sigma_{s,i}h_i}{4\pi}\phi_i^{n+1/2,l} + \frac{\sigma_{a,i}^{n+1/2,l}h_i}{4\pi}acT_i^{4,n+1/2,l} + 2Q_{i,m,L}^n + 2\mu_m\psi_{i-1/2,m}^{n+1/2,l+1/2} \\ \frac{\sigma_{s,i}h_i}{4\pi}\phi_i^{n+1/2,l} + \frac{\sigma_{a,i}^{n+1/2,l}h_i}{4\pi}acT_i^{4,n+1/2,l} + 2Q_{i,m,R}^n \end{bmatrix}, \end{aligned} \quad (A.3)$$

for  $\mu_m < 0$ :

$$\begin{aligned} \begin{bmatrix} -\mu_m + (\sigma_{t,i}^{n+1/2,l} + \frac{4}{c\Delta t_n})h_i & \mu_m \\ -\mu_m & -\mu_m + (\sigma_{t,i}^{n+1/2,l} + \frac{4}{c\Delta t_n})h_i \end{bmatrix} \begin{bmatrix} \psi_{i,m,L}^{n+1/2,l+1/2} \\ \psi_{i,m,R}^{n+1/2,l+1/2} \end{bmatrix} \\ = \begin{bmatrix} \frac{\sigma_{s,i}h_i}{4\pi}\phi_i^{n+1/2,l} + \frac{\sigma_{a,i}^{n+1/2,l}h_i}{4\pi}acT_i^{4,n+1/2,l} + 2Q_{i,m,L}^n \\ \frac{\sigma_{s,i}h_i}{4\pi}\phi_i^{n+1/2,l} + \frac{\sigma_{a,i}^{n+1/2,l}h_i}{4\pi}acT_i^{4,n+1/2,l} + 2Q_{i,m,R}^n - 2\mu_m\psi_{i+1/2,m}^{n+1/2,l+1/2} \end{bmatrix}. \end{aligned} \quad (A.4)$$

The right hand sides of Eqs. (A.3) and (A.4) are constructed with quantities from the previous low-order integration, the previous time step, and the previous step in the sweep solution process. In particular, the directionally-integrated intensity,  $\phi_i^{n+1/2,l}$ , and the temperature,  $T_i^{4,n+1/2,l}$ , come from the previous low-order iteration;  $Q_{i,m,L/R}^n$  comes from the previous time step, and the inflow angular intensity,  $\psi_{i+1/2,m}^{n+1/2,l+1/2}$  entering from the adjacent upwind cell is known from the previous step in the sweep solution process. By providing the incident intensity on the left boundary, the angular intensity for  $\mu_m > 0$  can be obtained by solving Eq. (A.3) from left to right. Also, providing the incident intensity on the right boundary, the angular intensity for  $\mu_m < 0$  can be obtained by solving Eq. (A.4) from right to left. With a source boundary condition these incident intensities are explicitly known, but for other boundary conditions such as a reflective condition, the incident intensities are implicitly expressed in terms of the exiting intensities, and may have to be iterated upon.

The variable Eddington factors needed in the low order system are computed at the cell edges as follows:

$$f_{i\pm 1/2}^{l+1/2} = \frac{\sum_{m=1}^M \mu_m^2 \psi_{i\pm 1/2,m}^{l+1/2} w_m}{\sum_{m=1}^M \psi_{i\pm 1/2,m}^{l+1/2} w_m}, \quad (\text{A.5})$$

where  $\psi_{i\pm 1/2,m}^{l+1/2}$  is defined by Eqs. (6.4a) and (6.4b). The Eddington factors are computed within cell  $i$  as follows:

$$f_{i,m}^{l+1/2}(x) = \frac{\sum_{m=1}^M \mu_m^2 \psi_{i,m}^{l+1/2}(x) w_m}{\sum_{m=1}^M \psi_{i,m}^{l+1/2}(x) w_m}, \quad x \in (x_{i-1/2}, x_{i+1/2}), \quad (\text{A.6})$$

where  $\psi_{i,m}^{l+1/2}(x)$  is defined by Eq. (6.1).

The same procedure can be applied for the second half time step, which yields for  $\mu_m > 0$ :

$$\begin{aligned} & \begin{bmatrix} \mu_m + (\sigma_{t,i}^{n+1,l} + \frac{3}{c\Delta t})h_i & \mu_m \\ -\mu_m & \mu_m + (\sigma_{t,i}^{n+1,l} + \frac{3}{c\Delta t})h_i \end{bmatrix} \begin{bmatrix} \psi_{i,m,L}^{n+1,l+1/2} \\ \psi_{i,m,R}^{n+1,l+1/2} \end{bmatrix} \\ &= \begin{bmatrix} \frac{\sigma_{s,i}h_i}{4\pi}\phi_i^{n+1,l} + \frac{\sigma_{a,i}^{n+1,l}h_i}{4\pi}acT_i^{4,n+1,l} + 2Q_{i,m,L}^n + 2Q_{i,m,L}^{n+1/2} + 2\mu_m\psi_{i-1,m,R}^{n+1,l+1/2} \\ \frac{\sigma_{s,i}h_i}{4\pi}\phi_i^{n+1,l} + \frac{\sigma_{a,i}^{n+1,l}h_i}{4\pi}acT_i^{4,n+1,l} + 2Q_{i,m,R}^n + 2Q_{i,m,R}^{n+1/2} \end{bmatrix}, \end{aligned} \quad (\text{A.7})$$

for  $\mu_m < 0$ :

$$\begin{aligned} & \begin{bmatrix} -\mu_m + (\sigma_{t,i}^{n+1,l} + \frac{3}{c\Delta t})h_i & \mu_m \\ -\mu_m & -\mu_m + (\sigma_{t,i}^{n+1,l} + \frac{3}{c\Delta t})h_i \end{bmatrix} \begin{bmatrix} \psi_{i,m,L}^{n+1,l+1/2} \\ \psi_{i,m,R}^{n+1,l+1/2} \end{bmatrix} \\ &= \begin{bmatrix} \frac{\sigma_{s,i}h_i}{4\pi}\phi_i^{n+1,l} + \frac{\sigma_{a,i}^{n+1,l}h_i}{4\pi}acT_i^{4,n+1,l} + 2Q_{i,m,L}^n + 2Q_{i,m,L}^{n+1/2} \\ \frac{\sigma_{s,i}h_i}{4\pi}\phi_i^{n+1,l} + \frac{\sigma_{a,i}^{n+1,l}h_i}{4\pi}acT_i^{4,n+1,l} + 2Q_{i,m,R}^n + 2Q_{i,m,R}^{n+1/2} - 2\mu_m\psi_{i+1,m,L}^{n+1,l+1/2} \end{bmatrix}, \end{aligned} \quad (\text{A.8})$$

where

$$Q_{i,m,L}^n = \frac{1}{4} \{-\mu_m(\psi_{i,m}^n - \psi_{i-1/2,m}^n) - \frac{h_i}{2}\sigma_{t,i}^n\psi_{i,m,L}^n + \frac{\sigma_{s,i}h_i}{8\pi}\phi_i^n + \frac{\sigma_{a,i}^nh_i}{8\pi}acT_i^{4,n}\}, \quad (\text{A.9a})$$

$$Q_{i,m,R}^n = \frac{1}{4} \{-\mu_m(\psi_{i+1/2,m}^n - \psi_{i,m}^n) - \frac{h_i}{2}\sigma_{t,i}^n\psi_{i,m,R}^n + \frac{\sigma_{s,i}h_i}{8\pi}\phi_i^n + \frac{\sigma_{a,i}^nh_i}{8\pi}acT_i^{4,n}\}, \quad (\text{A.9b})$$

$$\begin{aligned} Q_{i,m,L}^{n+1/2} &= \frac{1}{4} \{-\mu_m(\psi_{i,m}^{n+1/2} - \psi_{i-1/2,m}^{n+1/2}) + \frac{h_i}{2}(\frac{12}{c\Delta t} - \sigma_{t,i}^{n+1/2})\psi_{i,m,L}^{n+1/2} \\ &\quad + \frac{\sigma_{s,i}h_i}{8\pi}\phi_i^{n+1/2} + \frac{\sigma_{a,i}^{n+1/2}h_i}{8\pi}acT_i^{4,n+1/2}\}, \end{aligned} \quad (\text{A.10a})$$

$$\begin{aligned} Q_{i,m,R}^{n+1/2} &= \frac{1}{4} \{-\mu_m(\psi_{i+1/2,m}^{n+1/2} - \psi_{i,m}^{n+1/2}) + \frac{h_i}{2}(\frac{12}{c\Delta t} - \sigma_{t,i}^{n+1/2})\psi_{i,m,R}^{n+1/2} \\ &\quad + \frac{\sigma_{s,i}h_i}{8\pi}\phi_i^{n+1/2} + \frac{\sigma_{a,i}^{n+1/2}h_i}{8\pi}acT_i^{4,n+1/2}\}. \end{aligned} \quad (\text{A.10b})$$

## Appendix B. Spatial discretization for mixed finite-element Method

Applying the TR/BDF2 method for the time differencing scheme and the volumetric integration to Eq. (3.14) for the first half time step, we obtain:

$$\begin{aligned} h_i \frac{4C_{v,i}^{n+1/4}}{\Delta t} T_i^{n+1/2,l+1} &= h_i \sigma_{a,i}^{n+1/2,l} [\phi_i^{n+1/2,l+1} - acT_i^{n+1/2,l,4} \\ &\quad - 4acT_i^{n+1/2,l,3} (T_i^{n+1/2,l+1} - T_i^{n+1/2,l})] + h_i Q T_i^n, \end{aligned} \quad (\text{B.1})$$

where

$$Q T_i^n = \sigma_{a,i}^n (\phi_i^n - acT_i^{n,4}) + \frac{4C_{v,i}^{n+1/4}}{\Delta t} T_i^n. \quad (\text{B.2})$$

Algebraic manipulation of Eq. (B.1) yields the following expression for  $T_i^{n+1/2,l+1}$ :

$$T_i^{n+1/2,l+1} = \frac{\sigma_{a,i}^{n+1/2,l}(\phi_i^{n+1/2,l+1} + 3acT_i^{n+1/2,l,4}) + QT_i^n}{\frac{4C_{v,i}^{n+1/4}}{\Delta t} + 4\sigma_{a,i}^{n+1/2,l}acT_i^{n+1/2,l,3}}. \quad (\text{B.3})$$

Applying the same procedure for Eq. (3.12), we get:

$$\begin{aligned} & h_i \frac{4}{c\Delta t} \phi_i^{n+1/2,l+1} + F_{i,R}^{n+1/2,l+1} - F_{i,L}^{n+1/2,l+1} \\ &= h_i \sigma_{a,i}^{n+1/2,l} [acT_i^{n+1/2,l,4} + 4acT_i^{n+1,l,3} (T_i^{n+1/2,l+1} - T_i^{n+1/2,l}) - \phi_i^{n+1/2,l+1}] + Q\phi_i^n, \end{aligned} \quad (\text{B.4})$$

where

$$Q\phi_i^n = F_{i,L}^n - F_{i,R}^n + h_i \sigma_{a,i}^n (acT_i^{n,4} - \phi_i^n) + h_i \frac{4}{c\Delta t} \phi_i^n. \quad (\text{B.5})$$

Substituting Eq. (B.3), the expression for  $T_i^{n+1/2,l+1}$ , into Eq. (B.4), we have:

$$\begin{aligned} & h_i \left( \frac{4}{c\Delta t} + \sigma_{a,i}^{n+1/2,l} \frac{C_{v,i}^{n+1/4}/\Delta t}{\frac{C_{v,i}^{n+1/4}}{\Delta t} + A_i^{n+1/2,l}} \right) \phi_i^{n+1/2,l+1} + F_{i,R}^{n+1/2,l+1} - F_{i,L}^{n+1/2,l+1} \\ &= h_i \frac{A_i^{n+1/2,l}}{\frac{C_{v,i}^{n+1/4}}{\Delta t} + A_i^{n+1/2,l}} Q T_i^n - 3A_i^{n+1/2,l} h_i \frac{C_{v,i}^{n+1/4}/\Delta t}{\frac{C_{v,i}^{n+1/4}}{\Delta t} + A_i^{n+1/2,l}} T_i^{n+1/2,l} + Q\phi_i^n, \end{aligned} \quad (\text{B.6})$$

where  $A_i^{n+1/2,l} = \sigma_{a,i}^{n+1/2,l} acT_i^{n+1/2,l,3}$ .

Multiplying Eq. (3.13) by  $B_{i,L}(x)$ ,  $B_{i,R}(x)$ , and integrating over each cell, respectively, for the first half time integral, we obtain:

$$\begin{aligned} & \int_{x_{i-1/2}}^{x_{i+1/2}} B_{i,L}(x) \left\{ \frac{4}{c\Delta t} F^{n+1/2,l+1} + \frac{\partial}{\partial x} [f^{n+1/2,l+1/2} \phi^{n+1/2,l+1}] \right. \\ & \quad \left. + \sigma_t^{n+1/2,l} F^{n+1/2,l+1} + Q F^n \right\} dx = 0, \end{aligned} \quad (\text{B.7a})$$

$$\begin{aligned} & \int_{x_{i-1/2}}^{x_{i+1/2}} B_{i,R}(x) \left\{ \frac{4}{c\Delta t} F^{n+1/2,l+1} + \frac{\partial}{\partial x} [f^{n+1/2,l+1/2} \phi^{n+1/2,l+1}] \right. \\ & \quad \left. + \sigma_t^{n+1/2,l} F^{n+1/2,l+1} + Q F^n \right\} dx = 0, \end{aligned} \quad (\text{B.7b})$$

where

$$Q F^n = \frac{\partial}{\partial x} [f^n \phi^n] + \sigma_t^n F^n - \frac{4}{c\Delta t} F^n. \quad (\text{B.8})$$

Integrating by parts produces

$$\begin{aligned} & -f_{i-1/2}^{n+1/2,l+1/2} \phi_{i-1/2}^{n+1/2,l+1} + f_i^{n+1/2,l+1/2} \phi_i^{n+1/2,l+1} \\ & + \left( \frac{4}{c\Delta t} + \Sigma_{t,i}^{n+1/2,l} \right) h_i \left( \frac{F_{i,L}^{n+1/2,l+1}}{3} + \frac{F_{i,R}^{n+1/2,l+1}}{6} \right) + Q F_{i,L}^n = 0, \end{aligned} \quad (\text{B.9a})$$

$$\begin{aligned} & f_{i+1/2}^{n+1/2,l+1/2} \phi_{i+1/2}^{n+1/2,l+1} - f_i^{n+1/2,l+1/2} \phi_i^{n+1/2,l+1} \\ & + \left( \frac{4}{c\Delta t} + \Sigma_{t,i}^{n+1/2,l} \right) h_i \left( \frac{F_{i,L}^{n+1/2,l+1}}{6} + \frac{F_{i,R}^{n+1/2,l+1}}{3} \right) + Q F_{i,R}^n = 0, \end{aligned} \quad (\text{B.9b})$$

where

$$Q F_{i,L}^n = -f_{i-1/2}^n \phi_{i-1/2}^n + f_i^n \phi_i^n + \left( -\frac{4}{c\Delta t} + \Sigma_{t,i}^n \right) h_i \left( \frac{F_{i,L}^n}{3} + \frac{F_{i,R}^n}{6} \right), \quad (\text{B.10a})$$

$$Q F_{i,R}^n = f_{i+1/2}^n \phi_{i+1/2}^n - f_i^n \phi_i^n + \left( -\frac{4}{c\Delta t} + \Sigma_{t,i}^n \right) h_i \left( \frac{F_{i,L}^n}{6} + \frac{F_{i,R}^n}{3} \right). \quad (\text{B.10b})$$



The Eddington factors  $f$  are calculated using the angular intensities from the LLDG  $S_n$  step. Here  $f_{i\pm 1/2}$  is the cell edge Eddington factor, defined by Eq. (A.5), while  $f_i$  is the average over cell  $i$  of the Eddington factor, defined by Eq. (A.6). The spatial dependence of the Eddington factor within each cell takes the form of a rational polynomial, therefore, numerical quadratures are used for computing the average Eddington factor over each cell. In particular, two point Gauss quadrature was used:

$$f_i = \int_{x_{i-1/2}}^{x_{i+1/2}} f(x) dx \approx \frac{1}{2} [f(x_{i,L}^G) + f(x_{i,R}^G)], \quad (\text{B.11})$$

where

$$x_{i,L/R}^G = \frac{x_{i+1/2} + x_{i-1/2}}{2} \mp \frac{h_i}{2\sqrt{3}}. \quad (\text{B.12})$$

From Eqs. (B.9a) and (B.9b), we get the following expressions for  $F_{i,L}^{n+1/2,l+1}$  and  $F_{i,R}^{n+1/2,l+1}$ :

$$F_{i,L}^{n+1/2,l+1} = \frac{-2}{h_i(\frac{4}{c\Delta t} + \sigma_{t,i}^{n+1/2,l})} [-2f_{i-1/2}^{n+1/2,l+1/2} \phi_{i-1/2}^{n+1/2,l+1} + 3f_i^{n+1/2,l+1/2} \phi_i^{n+1/2,l+1} - f_{i+1/2}^{n+1/2,l+1/2} \phi_{i+1/2}^{n+1/2,l+1} + 2Q F_{i,L}^n - Q F_{i,R}^n], \quad (\text{B.13a})$$

$$F_{i,R}^{n+1/2,l+1} = \frac{-2}{h_i(\frac{4}{c\Delta t} + \sigma_{t,i}^{n+1/2,l})} [f_{i-1/2}^{n+1/2,l+1/2} \phi_{i-1/2}^{n+1/2,l+1} - 3f_i^{n+1/2,l+1/2} \phi_i^{n+1/2,l+1} + 2f_{i+1/2}^{n+1/2,l+1/2} \phi_{i+1/2}^{n+1/2,l+1} + 2Q F_{i,R}^n - Q F_{i,L}^n]. \quad (\text{B.13b})$$

Imposing continuity of flux on the interior cell boundary, we obtain:

$$F_{i,R}^{n+1/2,l+1} = F_{i+1,L}^{n+1/2,l+1}, \quad i = 1, \dots, I-1, \quad (\text{B.14})$$

which yields:

$$\begin{aligned} & \frac{-2}{h_i(\frac{4}{c\Delta t} + \sigma_{t,i}^{n+1/2,l})} [f_{i-1/2}^{n+1/2,l+1/2} \phi_{i-1/2}^{n+1/2,l+1} - 3f_i^{n+1/2,l+1/2} \phi_i^{n+1/2,l+1} \\ & \quad + 2f_{i+1/2}^{n+1/2,l+1/2} \phi_{i+1/2}^{n+1/2,l+1} + 2Q F_{i,R}^n - Q F_{i,L}^n] \\ &= \frac{-2}{h_{i+1}(\frac{4}{c\Delta t} + \sigma_{t,i+1}^{n+1/2,l})} [-2f_{i+1/2}^{n+1/2,l+1/2} \phi_{i+1/2}^{n+1/2,l+1} + 3f_{i+1}^{n+1/2,l+1/2} \phi_{i+1}^{n+1/2,l+1} \\ & \quad - f_{i+3/2}^{n+1/2,l+1/2} \phi_{i+3/2}^{n+1/2,l+1} + 2Q F_{i+1,L}^n - Q F_{i+1,R}^n]. \end{aligned} \quad (\text{B.15})$$

Also substituting the expression for  $F_{i,L}^{n+1/2,l+1}$  and  $F_{i,R}^{n+1/2,l+1}$  back into the discretized radiation energy equation, Eq. (B.6), leads to:

$$\begin{aligned} & \frac{-6f_{i-1/2}^{n+1/2,l+1/2}}{(\frac{4}{c\Delta t} + \sigma_{t,i}^{n+1/2,l})h_i} \phi_{i-1/2}^{n+1/2,l+1} \\ & + \left[ \frac{12f_i^{n+1/2,l+1/2}}{(\frac{4}{c\Delta t} + \sigma_{t,i}^{n+1/2,l})h_i} + h_i(\frac{4}{c\Delta t} + \sigma_{a,i}^{n+1/2,l}) \frac{C_{v,i}^{n+1/4}/\Delta t}{\frac{C_{v,i}^{n+1/4}}{\Delta t} + A_i^{n+1/2,l}} \right] \phi_i^{n+1/2,l+1} \\ & - \frac{6f_{i+1/2}^{n+1/2,l+1/2}}{(\frac{4}{c\Delta t} + \sigma_{t,i}^{n+1/2,l})h_i} \phi_{i+1/2}^{n+1/2,l+1} \\ & = h_i(\frac{A_i^{n+1/2,l}}{\frac{C_{v,i}^{n+1/4}}{\Delta t} + A_i^{n+1/2,l}}) Q T_i^n - 3A_i^{n+1/2,l} h_i \frac{C_{v,i}^{n+1/4}/\Delta t}{\frac{C_{v,i}^{n+1/4}}{\Delta t} + A_i^{n+1/2,l}} T_i^{n+1/2,l} + Q \phi_i^n \\ & \quad + \frac{6}{(\frac{4}{c\Delta t} + \sigma_{t,i}^{n+1/2,l})h_i} (Q F_{i,R}^n - Q F_{i,L}^n). \end{aligned} \quad (\text{B.16})$$

The equations for the outer boundary intensities  $\phi_{1/2}$  and  $\phi_{I+1/2}$  involve boundary conditions together with a continuity of flux condition. For example, the equation for  $\phi_{1/2}$  is

$$F_{1,L} = F_{1/2}, \quad (\text{B.17})$$

where  $F_{1,L}$  is defined by Eqs. (B.13a), and  $F_{1/2}$  is the left boundary flux. For a reflective condition,

$$F_{1/2} = 0. \quad (\text{B.18})$$

For a source condition,

$$F_{1/2} = 2F_{1/2}^+ - \left[ \frac{(F_{1/2}^+ + F_{1/2}^-)}{\phi_{1/2}} \right] \phi_{1/2} = 2 \sum_{\mu_m > 0} \mu_m \psi_{1/2,m} w_m - f_{1/2}^b \phi_{1/2}, \quad (\text{B.19})$$

where  $F^+ = 2\pi \int_0^1 \mu \psi d\mu$ ,  $F^- = -2\pi \int_{-1}^0 \mu \psi d\mu$ , and the boundary condition correction factor is given by

$$f_{1/2}^b = \frac{\sum_{m=1}^M |\mu_m| \psi_{1/2,m} w_m}{\sum_{m=1}^M \psi_{1/2,m} w_m}. \quad (\text{B.20})$$

The equation for  $\phi_{I+1/2}$  is

$$F_{I,R} = F_{I+1/2}, \quad (\text{B.21})$$

where  $F_{I,R}$  is defined by Eqs. (B.13b), and  $F_{I+1/2}$  is the right boundary flux defined by a boundary condition. For a reflective boundary condition,

$$F_{I+1/2} = 0. \quad (\text{B.22})$$

For a source condition,

$$F_{I+1/2} = \left[ \frac{(F_{I+1/2}^+ + F_{I+1/2}^-)}{\phi_{I+1/2}} \right] \phi_{I+1/2} - 2F_{I+1/2}^- = f_{I+1/2}^b \phi_{I+1/2} - 2 \sum_{\mu_m < 0} \mu_m \psi_{I+1/2,m} w_m, \quad (\text{B.23})$$

where

$$f_{I+1/2}^b = \frac{\sum_{m=1}^M |\mu_m| \psi_{I+1/2,m} w_m}{\sum_{m=1}^M \psi_{I+1/2,m} w_m}. \quad (\text{B.24})$$

Overall, we obtain  $2I + 1$  equations for the cell-center and cell-edge directionally-integrated intensities. This system of equations for the directionally-integrated intensities is SPD and can be solved by a banded matrix solver with a bandwidth five. Once the intensities have been computed, the temperatures are obtained via Eq. (B.3). The resultant cell-center directionally-integrated intensities and temperatures are used as an update to the LLDG  $S_n$  scattering and emission sources, respectively. Once the VEF iterations are converged, the radiative fluxes are obtained via Eqs. (B.13a) and (B.13b). The converged low-order solutions for the directionally-integrated intensities, the material temperatures, and the radiative fluxes are used as the final solutions at time step  $n + 1/2$ .

The same strategy can be applied to the second half time step. Here we only list the main equations for solving the low order system for the second half time step while neglecting the derivation process.

From the continuity of radiative fluxes at inner cell boundary and the radiation energy equation, we have:

$$\begin{aligned} & \frac{-2}{h_i(\frac{3}{c\Delta t} + \sigma_{t,i}^{n+1,l})} [f_{i-1/2}^{n+1,l+1/2} \phi_{i-1/2}^{n+1,l+1} - 3f_i^{n+1,l+1/2} \phi_i^{n+1,l+1} \\ & + 2f_{i+1/2}^{n+1,l+1/2} \phi_{i+1/2}^{n+1,l+1} + 2Q F_{i,R}^{n+1/2} - Q F_{i,L}^{n+1/2} + 2Q F_{i,R}^n - Q F_{i,L}^n] \\ & = \frac{-2}{h_{i+1}(\frac{3}{c\Delta t} + \sigma_{t,i+1}^{n+1,l})} [-2f_{i+1/2}^{n+1,l+1/2} \phi_{i+1/2}^{n+1,l+1} + 3f_{i+1}^{n+1,l+1/2} \phi_{i+1}^{n+1,l+1} \\ & - f_{i+3/2}^{n+1,l+1/2} \phi_{i+3/2}^{n+1,l+1} + 2Q F_{i,L+1}^{n+1/2} - Q F_{i+1,R}^{n+1/2} + 2Q F_{i+1,L}^n - Q F_{i+1,R}^n]. \end{aligned} \quad (\text{B.25})$$

$$\begin{aligned}
& -\frac{6f_{i-1/2}^{n+1,l+1/2}}{(\frac{3}{c\Delta t} + \sigma_{t,i}^{n+1,l})h_i}\phi_{i-1/2}^{n+1,l+1} \\
& + [\frac{12f_i^{n+1,l+1/2}}{(\frac{3}{c\Delta t} + \sigma_{t,i}^{n+1,l})h_i} + h_i(\frac{3}{c\Delta t} + \sigma_{a,i}^{n+1,l})\frac{3C_{v,i}^{n+3/4}/\Delta t}{\frac{3C_{v,i}^{n+3/4}}{\Delta t} + 4A_i^{n+1,l}}]\phi_i^{n+1,l+1} \\
& - \frac{6f_{i+1/2}^{n+1,l+1/2}}{(\frac{4}{c\Delta t} + \sigma_{t,i}^{n+1,l})h_i}\phi_{i+1/2}^{n+1,l+1} \\
& = h_i(\frac{4A_i^{n+1,l}}{\frac{3C_{v,i}^{n+3/4}}{\Delta t} + 4A_i^{n+1,l}})(Q T_i^{n+1/2} + Q T_i^n) - 3A_i^{n+1,l}h_i\frac{3C_{v,i}^{n+3/4}/\Delta t}{\frac{3C_{v,i}^{n+3/4}}{\Delta t} + 4A_i^{n+1,l}}T_i^{n+1,l} \\
& \quad + Q\phi_i^{n+1/2} + Q\phi_i^n \\
& \quad + \frac{6}{(\frac{3}{c\Delta t} + \sigma_{t,i}^{n+1,l})h_i}(Q F_{i,R}^{n+1/2} - Q F_{i,L}^{n+1/2} + Q F_{i,R}^n - Q F_{i,L}^n),
\end{aligned} \tag{B.26}$$

where

$$A_i^{n+1,l} = \sigma_{a,i}^{n+1,l} acT_i^{n+1,l,3}, \tag{B.27a}$$

$$Q\phi_i^{n+1/2} = \frac{1}{4}[F_{i,L}^{n+1/2} - F_{i,R}^{n+1/2} + h_i\sigma_{a,i}^{n+1/2}(acT_i^{n+1/2,4} - \phi_i^{n+1/2})] + h_i\frac{3}{c\Delta t}\phi_i^{n+1/2}, \tag{B.27b}$$

$$Q\phi_i^n = \frac{1}{4}[F_{i,L}^n - F_{i,R}^n + h_i\sigma_{a,i}^n(acT_i^{n,4} - \phi_i^n)], \tag{B.27c}$$

$$Q F_{i,L}^{n+1/2} = -\frac{1}{4}f_{i-1/2}^{n+1/2}\phi_{i-1/2}^{n+1/2} + \frac{1}{4}f_i^{n+1/2}\phi_i^{n+1/2} + (-\frac{3}{c\Delta t} + \frac{1}{4}\Sigma_{t,i}^{n+1/2})h_i(\frac{F_{i,L}^{n+1/2}}{3} + \frac{F_{i,R}^{n+1/2}}{6}), \tag{B.27d}$$

$$Q F_{i,R}^{n+1/2} = \frac{1}{4}f_{i+1/2}^{n+1/2}\phi_{i+1/2}^{n+1/2} - \frac{1}{4}f_i^{n+1/2}\phi_i^{n+1/2} + (-\frac{3}{c\Delta t} + \frac{1}{4}\Sigma_{t,i}^{n+1/2})h_i(\frac{F_{i,L}^{n+1/2}}{6} + \frac{F_{i,R}^{n+1/2}}{3}), \tag{B.27e}$$

$$Q F_{i,L}^n = -\frac{1}{4}f_{i-1/2}^n\phi_{i-1/2}^n + \frac{1}{4}f_i^n\phi_i^n + \frac{1}{4}\Sigma_{t,i}^nh_i(\frac{F_{i,L}^n}{3} + \frac{F_{i,R}^n}{6}), \tag{B.27f}$$

$$Q F_{i,R}^n = \frac{1}{4}f_{i+1/2}^n\phi_{i+1/2}^n - \frac{1}{4}f_i^n\phi_i^n + \frac{1}{4}\Sigma_{t,i}^nh_i(\frac{F_{i,L}^n}{6} + \frac{F_{i,R}^n}{3}). \tag{B.27g}$$

The expressions for  $F_{i,L}^{n+1,l+1}$  and  $F_{i,R}^{n+1,l+1}$  are as follows:

$$\begin{aligned}
F_{i,L}^{n+1,l+1} &= \frac{-2}{h_i(\frac{3}{c\Delta t} + \sigma_{t,i}^{n+1,l})}[-2f_{i-1/2}^{n+1,l+1/2}\phi_{i-1/2}^{n+1,l+1} + 3f_i^{n+1,l+1/2}\phi_i^{n+1,l+1} \\
& - f_{i+1/2}^{n+1,l+1/2}\phi_{i+1/2}^{n+1,l+1} + 2Q F_{i,L}^{n+1/2} - Q F_{i,R}^{n+1/2} + 2Q F_{i,L}^n - Q F_{i,R}^n],
\end{aligned} \tag{B.28a}$$

$$\begin{aligned}
F_{i,R}^{n+1,l+1} &= \frac{-2}{h_i(\frac{3}{c\Delta t} + \sigma_{t,i}^{n+1,l})}[f_{i-1/2}^{n+1,l+1/2}\phi_{i-1/2}^{n+1,l+1} - 3f_i^{n+1,l+1/2}\phi_i^{n+1,l+1} \\
& + 2f_{i+1/2}^{n+1,l+1/2}\phi_{i+1/2}^{n+1,l+1} + 2Q F_{i,R}^{n+1/2} - Q F_{i,L}^{n+1/2} + 2Q F_{i,R}^n - Q F_{i,L}^n].
\end{aligned} \tag{B.28b}$$

The expression of  $T_i^{n+1,l+1}$  is

$$T_i^{n+1,l+1} = \frac{\sigma_{a,i}^{n+1,l}(\phi_i^{n+1,l+1} + 3acT_i^{n+1,l,4}) + Q T_i^{n+1/2} + Q T_i^n}{\frac{3C_{v,i}^{n+3/4}}{\Delta t} + 4\sigma_{a,i}^{n+1,l}acT_i^{n+1,l,3}}, \tag{B.29}$$

where

$$Q T_i^{n+1/2} = \frac{1}{4}[\sigma_{a,i}^{n+1/2}(\phi_i^{n+1/2} - acT_i^{n+1/2,4})] + \frac{3C_{v,i}^{n+3/4}}{\Delta t}T_i^{n+1/2}, \tag{B.30a}$$

$$Q T_i^n = \frac{1}{4}[\sigma_{a,i}^n(\phi_i^n - acT_i^{n,4})]. \tag{B.30b}$$

## References

- [1] V.Y. Gol'din, A quasi-diffusion method of solving the kinetic equation, *USSR Comput. Math. Math. Phys.* 4 (1967) 136–149.
- [2] E.N. Aristova, V.Y. Gol'din, A.V. Kolpakov, Multidimensional calculations of radiation transport by nonlinear quasi-diffusion method, in: *Proc. Int. Conf. Mathematics and Computation, Reactor Physics and Environmental Analysis in Nuclear Applications*, Madrid, Spain, American Nuclear Society, 1991.
- [3] E.N. Aristova, Simulation of radiation transport in a channel based on the quasi-diffusion method, *Transp. Theory Stat. Phys.* 37 (5–7) (2008) 483–503.
- [4] M. Adams, E. Larsen, Fast iterative methods for discrete-ordinates particle transport calculations, *Prog. Nucl. Energy* 40 (1) (2002) 3–159.
- [5] R. Alcouffe, Diffusion synthetic acceleration methods for the diamond-differenced discrete-ordinates equations, *Nucl. Sci. Eng.* 64 (1977) 344–355.
- [6] J. Warsa, T. Wareing, J. Morel, Fully-consistent diffusion-synthetic acceleration of linear discontinuous  $S_n$  transport discretizations on unstructured tetrahedral meshes, *Nucl. Sci. Eng.* 141 (2002) 235–251.
- [7] J. Morel, E. Larsen, A multiple balance approach for differencing the  $S_n$  equations, *Nucl. Sci. Eng.* 105 (1990) 1–15.
- [8] M.L. Adams, W.R. Martin, Diffusion synthetic acceleration of discontinuous finite element transport iterations, *Nucl. Sci. Eng.* 111 (1992) 145–167.
- [9] Y. Wang, J.C. Ragusa, Diffusion synthetic acceleration for high-order discontinuous finite element  $S_n$  transport schemes and application to locally refined unstructured meshes, *Nucl. Sci. Eng.* 166 (2) (2010) 145–166.
- [10] E.W. Larsen, J. Morel, J. Warren, F. Miller, Asymptotic solutions of numerical transport problems in optically thick, diffusive regimes, *J. Comput. Phys.* 69 (1987) 283–324.
- [11] J.D. Edwards, J.E. Morel, D.A. Knoll, Nonlinear variants of the TR/BDF2 method for thermal radiative diffusion, *J. Comput. Phys.* 230 (2011) 1198–1214.
- [12] S.S. Olivier, J.E. Morel, Variable Eddington factor method for the  $s_n$  equations with lumped discontinuous Galerkin spatial discretization coupled to a drift-diffusion acceleration equation with mixed finite-element discretization, *J. Comput. Theor. Transp.* 46 (6–7) (2018) 480–496.
- [13] V. Dobrev, T. Kolev, R. Rieben, High-order curvilinear finite element methods for Lagrangian hydrodynamics, *SIAM J. Sci. Comput.* 34 (2012) B606–B641.
- [14] S. Bolding, J. Hansel, J.D. Edwards, J.E. Morel, R.B. Lowrie, Second-order discretization in space and time for radiation-hydrodynamics, *J. Comput. Phys.* 338 (2017) 511–526.
- [15] N. Gentile, N. Keen, J. Rathkopf, The Kull IMC Package, Lawrence Livermore National Laboratory (LLNL), Livermore, CA, 1998, Technical report uclrl-jc-132743 edition.
- [16] J. Morel, T. Wareing, K. Smith, A linear-discontinuous spatial differencing scheme for  $s_n$  radiative transfer calculation, *J. Comput. Phys.* 128 (1996) 445–462.
- [17] A. Wollaber, Four decades of Implicit Monte Carlo, *J. Comput. Theor. Transp.* 45 (2016) 1–70.